



HAL
open science

Representation of Diabatic Potential Energy Matrices for Multiconfiguration Time-Dependent Hartree Treatments of High-Dimensional Nonadiabatic Photodissociation Dynamics

Shanyu Han, Markus Schröder, Fabien Gatti, Hans-Dieter Meyer, David
Lauvergnat, David Yarkony, Hua Guo

► **To cite this version:**

Shanyu Han, Markus Schröder, Fabien Gatti, Hans-Dieter Meyer, David Lauvergnat, et al.. Representation of Diabatic Potential Energy Matrices for Multiconfiguration Time-Dependent Hartree Treatments of High-Dimensional Nonadiabatic Photodissociation Dynamics. *Journal of Chemical Theory and Computation*, 2022, 18 (8), pp.4627-4638. 10.1021/acs.jctc.2c00370 . hal-03774051

HAL Id: hal-03774051

<https://hal.science/hal-03774051>

Submitted on 15 Nov 2022

HAL is a multi-disciplinary open access archive for the deposit and dissemination of scientific research documents, whether they are published or not. The documents may come from teaching and research institutions in France or abroad, or from public or private research centers.

L'archive ouverte pluridisciplinaire **HAL**, est destinée au dépôt et à la diffusion de documents scientifiques de niveau recherche, publiés ou non, émanant des établissements d'enseignement et de recherche français ou étrangers, des laboratoires publics ou privés.

**Multiconfiguration time-dependent Hartree approach to high-dimensional
nonadiabatic photodissociation dynamics**

Shanyu Han,^a Markus Schröder,^b Fabien Gatti,^c Hans-Dieter Meyer,^b David Lauvergnat^d,

David R. Yarkony,^e and Hua Guo^{a,*}

^aDepartment of Chemistry and Chemical Biology, University of New Mexico,

Albuquerque, New Mexico 87131, USA

^bTheoretische Chemie, Physikalisch Chemisches Institut, Ruprecht-Karls Universität

Heidelberg, D-69120 Heidelberg, Germany

^cISMO, Institut des Sciences Moléculaires d'Orsay - UMR 8214 CNRS/Université Paris-

Saclay, F-91405 Orsay, France

^dUniversité Paris-Saclay, CNRS, Institut de Chimie Physique UMR8000, Orsay 91405,

France

^eDepartment of Chemistry, Johns Hopkins University, Baltimore, Maryland 21218, USA

*: corresponding author: hguo@unm.edu

Abstract

Conventional quantum mechanical characterization of photodissociation dynamics is restricted by steep scaling laws with respect to the dimensionality of the system. In this work, we examine the applicability of the multi-configurational time-dependent Hartree (MCTDH) method in treating nonadiabatic photodissociation dynamics in two prototypical systems, taking advantage of its favorable scaling laws. To conform to the sum-of-product form, elements of the ab initio diabatic potential energy matrix (DPEM) are re-expressed using the recently proposed Monte Carlo canonical polyadic decomposition method, with enforcement of proper symmetry. The MCTDH absorption spectra and product branching ratios are shown to compare well with those calculated using conventional grid-based methods, demonstrating its promise for treating high-dimensional nonadiabatic photodissociation problems.

I. Introduction

The Born-Oppenheimer (BO) approximation¹ is an important pillar in understanding chemical transformation, because it greatly simplifies the quantum mechanical description of molecular systems by allowing the separation of nuclear and electronic degrees of freedom (DOFs). This adiabatic approximation, justified by the fact that the electron mass is so much smaller than that of a nucleus, forms the foundation of modern quantum chemistry in which the electronic Schrödinger equation is solved at fixed nuclear geometries. For room temperature spectroscopic and dynamic problems, it is often sufficient to include only the ground electronic state. However, it is now increasingly acknowledged that the BO approximation fails in many processes where excited electronic states are involved, leading to transitions between different electronic states.²⁻⁶ Even for a ground-state process, a high-lying excited state might still exert a non-negligible effect through a conical intersection (CI),⁷ even when the energy of the system is below the minimum energy crossing.^{8,9} These nonadiabatic processes are essential in understanding many chemical reactions, particularly those involving photoexcitation, such as radiationless decay,¹⁰ vision,¹¹ photodamage of DNAs,¹² and charge separation.¹³ Much recent effort has been devoted to a better understanding of nonadiabatic dynamics and photodissociation has served as a popular test ground.¹⁴⁻²¹

Theoretically, photodissociation dynamics can be characterized by solving the nuclear Schrödinger equation on a single or multiple coupled potential energy surfaces (PESs).^{14,}

¹⁶ In recent years, significant advances have been made in constructing PESs and multi-dimensional diabatic potential energy matrices (DPEMs) from high-level ab initio calculations,²²⁻²⁷ which have enabled quantum mechanical characterization of nonadiabatic photodissociation dynamics of important prototypes.^{20, 26} However, such first-principles description of photodissociation dynamics, particularly that based on an expansion on a grid or a basis, remains challenging for high-dimensional systems because the computational costs (both memory and CPU time) increase exponentially with the size of the problem. Because of this so-called curse of dimensionality, most such quantum mechanical investigations of photodissociation dynamics have been restricted to small (<9) dimensions,²⁶ which may not be sufficient to describe dynamics quantitatively in molecules with more than four atoms.

Over the past decades, many attempts have been made to overcome the curse of dimensionality. Perhaps the most promising example is the multi-configuration time-dependent Hartree (MCTDH) method,²⁸⁻³⁰ initially proposed 30 years ago.^{31, 32} MCTDH expresses the wave function as a sum of products (SOP) of the so-called single particle functions (SPFs), which greatly reduces the memory need for storing the wave function. Both the expansion coefficients and the SPFs are allowed to vary with time, governed by variationally determined time-dependent equations of motion. The most attractive feature of MCTDH is the use of adaptive basis, a consequence of which its scaling laws with the size of the problem are much more favorable than those for conventional fixed grid/basis

based methods. In principle, MCTDH is capable of handling much larger systems than conventional quantum methods, especially with the multi-layer version (ML-MCTDH).³³ This advantage has been amply demonstrated in several recent examples.³⁴⁻³⁹

However, the MCTDH wave function prefers the Hamiltonian to be expressed in the same SOP form, in order to attain the optimal efficiency, although alternative implements of the MCTDH algorithm avoiding the SOP restriction, such as the correlated DVR (CDVR) scheme⁴⁰ and the collocation approach,⁴¹ have also been proposed. The kinetic energy operator (KEO) typically fulfils the requirement, while the potential energy operator (PEO) often needs extra effort to conform to the SOP form. Several methods have been developed, among which POTFIT^{42, 43} and its variants⁴⁴⁻⁴⁷ are shown to be quite successful. However, the POTFIT method is based on the Tucker decomposition,⁴⁸ in which the scaling is still exponential. So the transformation of the PEO is often the bottleneck that prevents the application of MCTDH to high-dimensional systems. Recently, a new method, namely Monte Carlo canonical polyadic decomposition (MCCPD),⁴⁹ was proposed and successfully implemented for calculating the vibrational energy levels of a benchmark heptatomic system H_5O_2^+ known as the Zundel cation. Comparing to the exponential scaled Tucker decomposition, CPD has almost linear scaling, thus serving as a promising alternative to the PEO transformation in high-dimensional systems. Its efficiency is further improved by MC sampling. In a recent MCTDH study on carbon monoxide scattering from

Cu(100),³⁹ for example, MCCPD was successfully implemented to decompose a 21-dimensional PES.

Most existing MCTDH studies have dealt with dynamics on a single electronic state. In more recent work,⁵⁰ its capability to handle state-to-state inelastic scattering has been validated by comparing with previous exact time-independent studies. Many MCTDH studies on non-adiabatic dynamics (Refs. ^{35, 51-55} to name a few) are based on vibronic-coupling (VC) Hamiltonian,⁶ which is already in the SOP form. However, VC Hamiltonian cannot describe dissociative process, which demands ab initio determined coupled PESs. There have been few MCTDH treatments of nonadiabatic photodissociation processes with ab initio determined coupled PESs,⁵⁶⁻⁶¹ because the difficulties of representing the PESs and their couplings in the SOP form are compounded by the necessity for treating multiple electronic states. Because of the large phase space associated with photoexcited systems, chaotic dynamics may significantly affect the convergence of MCTDH, casting doubt on its applicability in such problems. This is a particularly acute challenge in systems affected by long-lived resonances. In this work, we examine the application of MCTDH in nonadiabatic photodissociation in two prototypical systems in order to shed light on its applicability in high-dimensional systems.

The two test cases investigated in this work are the photodissociation of ammonia (NH₃) in the first band and the hydroxymethyl radical (CH₂OH) in the 3s Rydberg state. In both cases, the excited and ground states are coupled by a CI seam, as shown in Figure 1.

Extensive studies on the former have been reported by us using a full-dimensional grid-based quantum method⁶²⁻⁶⁷ on accurate two-state DPEMs.^{63, 68} Excellent agreement with experiment⁶⁹⁻⁷⁴ has been achieved, underscoring the accuracy of these ab initio based DPEMs. Although there has also been a full-dimensional MCTDH study of this system,⁶⁰ the agreement with the absorption spectrum calculated using the standard grid based method⁶² on the same DPEM was not completely satisfactory. In the hydroxymethyl case, the photodissociation dynamics has also been investigated by us previously using reduced-dimensional models^{75, 76} on a full-dimensional ab initio DPEM.⁷⁷ The agreement with experiment^{78, 79} was also quite satisfactory. The existence of experimental and previous theoretical studies makes these two systems an ideal proving ground for MCTDH studies.

In this work, MCTDH was used to calculate the absorption spectrum and product branching ratio of the two photodissociation processes. In both systems, the elements of the DPEMs were refit to the SOP form using the MCCPD approach. Special attention is paid to enforce the permutation symmetry of the systems, which is vital for providing an accurate characterization of the nonadiabatic dynamics. Although NH_3 has ‘only’ six DOFs, it is quite challenging for MCTDH due to its long-lived resonances on the excited state PES, which require long-time propagation, leading to accumulation of errors. We demonstrate that MCTDH is capable of calculating the absorption spectrum accurately and the $\text{NH}_2(\text{A})/\text{NH}_2(\text{X})$ branching ratio to a lesser extent. For CH_2OH , the high dimensionality is the challenge. The calculated absorption spectrum is in reasonably good agreement with

our recent work using a reduced-dimensional model^{75, 76} and consistent with available experimental data.⁷⁸ With these two successful demonstrations, we establish the usefulness of the MCTDH method in treating nonadiabatic photodissociation dynamics in high-dimensional systems. This work is organized as follows. Section II outlines the theoretical methods and their implementation. The results are presented and discussed in Section III. A short summary is given in Section IV.

II. Methods

A. MCTDH

In MCTDH,^{31, 32} the time-dependent wave function for a system with f DOFs is expressed as sums of products (SOPs) of low-dimensional basis functions:

$$\begin{aligned}\Psi(q_1, \dots, q_f, t) &\equiv \Psi(Q_1, \dots, Q_m, t) = \sum_{j_1=1}^{n_1} \cdots \sum_{j_m=1}^{n_m} A_{j_1, \dots, j_m}(t) \prod_{\kappa=1}^m \varphi_{j_\kappa}^{(\kappa)}(Q_\kappa, t) \\ &= \sum_J \mathbf{A}_J \Phi_J,\end{aligned}\tag{1}$$

where q_1, \dots, q_f are one-dimensional nuclear coordinates and Q_1, \dots, Q_m are generalized coordinates with each Q_κ consisting of either a single or multiple nuclear coordinates. The latter is known as mode combination.⁸⁰ Note that the choice of the coordinates is system-dependent and can significantly impact the efficiency of the MCTDH calculations. $\mathbf{A}_J \equiv A_{j_1, \dots, j_m}$ are time-dependent expansion coefficients and Φ_J are products of the time-dependent single particle functions (SPFs) $\varphi_{j_\kappa}^{(\kappa)}(Q_\kappa, t)$, where the index denotes the j_κ th

SPF for the κ th mode. The SPFs are further represented by linear-combinations of time-independent primitive basis functions or grids.

The equations of motion for \mathbf{A}_J and $\varphi_{j_\kappa}^{(\kappa)}$ are derived from the Dirac-Frenkel variational principle and given by:

$$i\dot{\mathbf{A}}_J = \sum_L \langle \Phi_J | \mathbf{H} | \Phi_L \rangle \mathbf{A}_L, \quad (2a)$$

$$i\dot{\boldsymbol{\Phi}}^{(\kappa)} = (1 - \mathbf{P}^{(\kappa)}) (\boldsymbol{\rho}^{(\kappa)})^{-1} \langle \mathbf{H} \rangle^{(\kappa)} \boldsymbol{\Phi}^{(\kappa)}, \quad (2b)$$

$\boldsymbol{\Phi}^{(\kappa)} = (\varphi_1^{(\kappa)}, \dots, \varphi_{n_\kappa}^{(\kappa)})^T$. The Hamiltonian \mathbf{H} is system-dependent and defined below. $\langle \mathbf{H} \rangle^{(\kappa)}$, $\boldsymbol{\rho}^{(\kappa)}$ are the mean-field matrix and the density matrix, respectively:

$$\begin{aligned} \langle \mathbf{H} \rangle_{ab}^{(\kappa)} &= \sum_{j_1} \dots \sum_{j_{\kappa-1}} \sum_{j_{\kappa+1}} \dots \sum_{j_m} A_{j_1 \dots j_{\kappa-1} j_{\kappa+1} \dots j_m}^* \\ &\times \langle \varphi_{j_1}^{(\kappa)} \dots \varphi_{j_{\kappa-1}}^{(\kappa)} \varphi_{j_{\kappa+1}}^{(\kappa)} \varphi_{j_m}^{(\kappa)} | \mathbf{H} | \varphi_{j_1}^{(\kappa)} \dots \varphi_{j_{\kappa-1}}^{(\kappa)} \varphi_{j_{\kappa+1}}^{(\kappa)} \varphi_{j_m}^{(\kappa)} \rangle A_{j_1 \dots j_{\kappa-1} j_{\kappa+1} \dots j_m}, \end{aligned} \quad (3a)$$

$$\rho_{jl}^{(\kappa)} = \sum_{j_1} \dots \sum_{j_{\kappa-1}} \sum_{j_{\kappa+1}} \dots \sum_{j_m} A_{j_1 \dots j_{\kappa-1} j_{\kappa+1} \dots j_m}^* A_{j_1 \dots j_{\kappa-1} j_{\kappa+1} \dots j_m}. \quad (3b)$$

Where the origin of the SOP form is evident.

$\mathbf{P}^{(\kappa)}$ is a projection operator for the space spanned by the SPFs:

$$\mathbf{P}^{(\kappa)} = \sum_i |\varphi_i^{(\kappa)}\rangle \langle \varphi_i^{(\kappa)}|. \quad (4)$$

Detailed derivations of these equations can be found in a review²⁸ and more comprehensively in a recent book,²⁹ so are not given here.

B. Expressing DPEM with MCCPD

i. MCCPD

The Hamiltonian is required to be in the SOP form for efficiency, especially for high-dimensional problems. As mentioned above, the KEO typically assumes naturally this form, but the PEO needs be refit. In this work, the newly proposed MCCPD method⁴⁹ was implemented for the latter. We first consider a scalar PEO, which could be either an adiabatic PES or an element of a DPEM. This multi-dimensional function of the chosen coordinates can be approximated in MCCPD by canonical polyadic decomposition (CPD):⁴⁹

$$V(q_1, \dots, q_f) \equiv V(Q_1, \dots, Q_m) \approx V^{CPD}(Q_1, \dots, Q_m) = \sum_{r=1}^R c_r v_r^{(1)}(Q_1) \cdots v_r^{(m)}(Q_m). \quad (5)$$

Note that the relations between q_1, \dots, q_f and Q_1, \dots, Q_m are the same as define above. Here R is the rank of the CPD tensor, c_r is the expansion coefficient and $v_r^{(\kappa)}(Q_\kappa)$ is a one-dimensional function dependent only on coordinate Q_κ , which is called the single particle potential (SPP). The SPPs are assumed to be normalized but not necessarily orthogonal.

In a grid representation, the SPPs become vectors and PEO a tensor of rank R :

$$V_{i_1, \dots, i_\kappa, \dots, i_m} = \sum_{r=1}^R c_r v_{i_1, r}^{(1)} \cdots v_{i_\kappa, r}^{(\kappa)} \cdots v_{i_m, r}^{(m)}, \quad (6)$$

where i_κ denotes the i th grid point of the κ th mode. The grid points are commonly chosen as discrete variable representation (DVR)⁸¹ points of the corresponding mode. The alternating least squares (ALS) algorithm can be used to obtain both the coefficients and SPPs by minimizing the following functional for each mode:⁴⁹

$$J_\kappa = \sum_I W_I^\kappa (V_I - V_I^{CPD})^2 + \varepsilon \sum_r c_r^2 \sum_I W_I^\kappa \Omega_{r,I}^2, \quad (7)$$

with the additional definition $\Omega_{r,I} = \prod_\kappa v_r^{(\kappa)} (Q_\kappa^{i_\kappa})$, where the subscript I is a combined index of the i_κ as: $I = (i_1, \dots, i_m)$. W_I^κ is a positive and coordinate-dependent weight function. The weight function is used to emphasize important regions of the PES where high accuracy is needed and also serves as a distribution function of sampling points when the complete sum over I is later replaced by Monte Carlo sampling. Finally, a regularization parameter, ε , is introduced to prevent potentially ill-conditioned matrices in minimization.

To minimize J_κ , its functional derivative with respect to one SPP and coefficient of the i_κ grid is given as:

$$\frac{\delta J_\kappa}{\delta c_r v_{i_\kappa, r}^{(\kappa)}} = -2 \sum_{I^\kappa} W_{I^\kappa}^\kappa V_{I^\kappa} \Omega_{r, I^\kappa}^\kappa + 2 \sum_{r'} c_{r'} v_{i_\kappa, r'}^{(\kappa)} S_{r, r'}^\kappa + 2 \varepsilon c_r v_{i_\kappa, r}^{(\kappa)} S_{r, r}^\kappa \rightarrow 0, \quad (8)$$

where the abbreviations $S_{r, r'}^\kappa = \sum_{I^\kappa} W_{I^\kappa}^\kappa \Omega_{r, I^\kappa}^\kappa \Omega_{r', I^\kappa}^\kappa$ and $\Omega_{r, I^\kappa}^\kappa = \prod_{\kappa' \neq \kappa} v_{i_{\kappa'}, r}^{(\kappa')}$ have been used. This

leads to the following working equation:

$$\sum_{I^\kappa} W_{I^\kappa}^\kappa V_{I^\kappa} \Omega_{r, I^\kappa}^\kappa = \sum_{r'} S_{r, r'}^\kappa [1 + \varepsilon \delta_{r, r'}] c_{r'} v_{i_\kappa, r'}^{(\kappa)}, \quad (9)$$

for obtaining the SPPs and expansion coefficients.

Note the solution of Eq. (9) for mode κ depends on the solutions of all other DOFs, thus it must be done iteratively. The Monte Carlo (MC) method is used in calculating the multi-dimensional quadrature over I^κ . In the MC approach, the weight functions serve as the distribution function of the sampling points $\{\zeta^\kappa\}$, which are drawn randomly from the quadrature points $\{I^\kappa\}$. Thus $S_{r, r'}^\kappa$ and Eq. (9) can be evaluated as:

$$S_{r,r'}^\kappa \approx \sum_{\zeta^\kappa} \Omega_{r,\zeta^\kappa}^\kappa \Omega_{r',\zeta^\kappa}^\kappa, \quad (10)$$

$$\sum_{\zeta^\kappa} V_{i_\kappa,\zeta^\kappa} \Omega_{r,\zeta^\kappa}^\kappa \approx \sum_{r'} S_{r,r'}^\kappa [1 + \varepsilon \delta_{r,r'}] c_r v_{i_\kappa,r'}^{(\kappa)}, \quad (11)$$

Note that the MC sampling is applied to all modes except κ , but all quadrature points for κ th mode are included. Naturally, the quality of the minimization depends largely on the sampling of the quadrature points. The details of the minimization algorithm can be found in Ref. ⁴⁹.

Two kinds of sampling methods were proposed in MCCPD. One is called uniform MC sampling with equal weight ($W=1$) for all quadrature points. The other is the Metropolis MC sampling, in which the choice of the quadrature points is weighted by the Boltzmann factor $W=\exp(-E/k_B T)$, with k_B and T as the Boltzmann constant and hypothetical temperature in Kelvin. This Metropolis method is useful for systems near potential wells, as lower energy points are sampled more frequently. However, it may not be optimal for photodissociation because the dynamics explores a large phase space. In addition, fit PESs might contain artificial holes at unphysical structures, due to the lack of ab initio points. The Boltzmann weight can easily result in bias towards these regions, leading to poor convergence. Thus, an optimal way is to take advantages of both methods, using the former to cover the dissociative pathway and the latter for important local regions.

ii. Permutation symmetry adaptation

An important issue is concerned with the complete nuclear permutation and inversion (CNPI) symmetry⁸² for systems containing identical nuclei, such as NH₃. As the symmetry

operators commute with the Hamiltonian, symmetry adaptation is both advantageous and necessary for the evolution of the nuclear wave function. For NH₃, for example, the parity is used to label the ground state tunneling doublet and predissociative resonances on the excited state that form the peaks in the absorption spectrum. The permutation symmetry of the diagonal/off-diagonal terms of the DPEM for this system has been extensively discussed in the past.^{63, 77, 83} While the diagonal terms of the DPEMs are totally symmetric, the off-diagonal terms are antisymmetric with respect to the exchange of two H atoms. The symmetrization of the former is enforced in MCCPD as discussed below,⁴⁹ but the latter needs a special treatment to impose the antisymmetry.

$$V_i^{CPD} = \hat{P}_i V^{CPD}, \quad (12)$$

where \hat{P}_i is the symmetry projection operator for the i th irrep:

$$\hat{P}_i = \frac{1}{N_{sym}} \sum_n^{N_{sym}} \Gamma^i(G_n) \hat{G}_n, \quad (13)$$

where N_{sym} is the number of group elements, \hat{G}_n and $\Gamma^i(G_n)$ are the group operator and character for the corresponding group element G_n in the i th irrep. If the coordinate system

is amenable to the symmetry operations of a CNPI group, the element of the tensor has a one-to-one mapping under the action of \hat{G}_n . This is realized by the following form:

$$\hat{\Omega}_n = \hat{\omega}_n \prod_{\kappa} \hat{\omega}_{\kappa,n}, \quad (14)$$

where $\hat{\omega}_{\kappa,n}$ is a symmetry operator that exclusively operates on the DOFs within the mode κ and the operator $\hat{\omega}_n$ consecutively performs operations between different modes.

Additional rules can be introduced for efficient implementation of symmetry projection on a tensor in the CPD form. Since the final symmetrized tensor V_i^{CPD} has a total rank R , we can generate it with the following procedure. We start with l terms of $c_r \prod_{\kappa} v_{i_{\kappa},r}^{(\kappa)}$, $r = 1 \sim l$, where $l = \frac{R}{N_{sym}}$. The action of each $\hat{\Omega}_n$ on these terms will result in l additional terms, so that the final rank of the symmetrized tensor V_i^{CPD} defined in Eqs. (12) and (13) remains to be R . The symmetrization is performed at each minimization MCCPD step, as described in Ref. 49.

For each symmetry operator, one can express how $\Gamma^i(\Omega_n)\hat{\Omega}_n$ acts on a particular r th term for l th element of the CPD tensor V_l as:

$$\Gamma^i(\Omega_n)\hat{\omega}_n \prod_{\kappa} \hat{\omega}_{\kappa,n} c_r \prod_{\kappa} v_{i_{\kappa},r}^{(\kappa)} = c_r v_{j_{l},r'}^{(l)} \cdots \left(\Gamma^i(\Omega_n) v_{j_{\kappa},r'}^{(\kappa)} \right) \cdots v_{j_m,r'}^{(m)}, \quad (15)$$

with $r' = r + (n-1)l$,

$$\hat{\omega}_n v_{i_{\kappa},r}^{(\kappa)} = v_{j_{\kappa'},r'}^{(\kappa')} \quad \text{and} \quad \hat{\omega}_{\kappa,n} v_{i_{\kappa},r}^{(\kappa)} = v_{j_{\kappa},r'}^{(\kappa)}. \quad (16)$$

where the $\kappa \rightarrow \kappa'$ and $i_{\kappa} \rightarrow j_{\kappa'}$ mapping in the first equation and the $i_{\kappa} \rightarrow j_{\kappa}$ mapping in the second equation are defined by the symmetry operators of a specific system. Besides,

when $\Gamma^i(\Omega_n) = -1$, where to put the factor -1 depends on the coordinate system and mode combination. The detailed implementation for NH_3 and CH_2OH can be found in Table S2 and Table S3, respectively.

The symmetry adaptation in the original MCCPD method was restricted to the totally symmetric irrep, but the strategy can be readily extended to non-totally symmetric irreps, as discussed above. We emphasize that symmetry adaptation is only possible with a proper choice of the coordinate system. Since chemical bond cleavage is a necessity in photodissociation, it is often difficult to define a coordinate system that can fully take advantage of the CNPI symmetry. Under such circumstances, one can work with a subgroup in symmetry adaptation.

C. Coordinates and Hamiltonians

The nuclear Hamiltonian defined in a diabatic representation for characterizing the nonadiabatic dynamics of NH_3 or CH_2OH is given in the general matrix form:

$$\mathbf{H} = \hat{\mathbf{T}} + \mathbf{V}, \quad (15)$$

where \mathbf{I} is a 2×2 identity matrix and \mathbf{V} is the 2×2 DPDM, $\mathbf{V} = \begin{pmatrix} V_{11} & V_{12} \\ V_{21} & V_{22} \end{pmatrix}$. The existing

DPEMs of ammonia⁶³ and hydroxymethyl⁷⁷ were determined by a simultaneous fitting-and-diabatizing approach²⁶ from high quality ab initio data, including energies, gradients and derivative couplings, with proper adaption of CNPI symmetry. They are transformed

to the SOP form by decomposing the diagonal and off-diagonal terms separately using the MCCPD algorithm discussed above.

The (2+1) Radau-Jacobi coordinates⁸⁴ are used for NH₃. As shown in Figure 1, \vec{r}_1 and \vec{r}_2 are two Radau vectors and \vec{r}_3 is a Jacobi vector which defines the z axis of the body-fixed (BF) frame. $r_{i=1,3}$ and $\mu_{i=1-3}$ are the length and mass factor for the corresponding vector \vec{r}_i , respectively. θ_1 (θ_2) is the polar angle between \vec{r}_1 (\vec{r}_2) and \vec{r}_3 . ϕ is the relative azimuthal angle between the two Radau vectors in the BF frame. Here $u_{i=1,2}$ and $v_{i=1,2}$ are defined as $u_i = \cos(\theta_i)$ and $v_i = \sin(\theta_i)$, $i = 1, 2$. The machine readable form of the KEO is given in SI. While this coordinate system is not amenable to full CNPI group, it is suitable for a subgroup, as discussed SI in detail. We emphasize that this coordinate system is superior to the Jacobi coordinate systems used in the previous full-dimensional MCTDH calculation,⁶⁰ because symmetry adaptation can be enforced to resolve the two parities.

$$\vec{R}_i$$

$\vec{R}_i = (R_i, \theta_i, \varphi_i)$. Likewise, we define $u_i = \cos(\theta_i)$. The central vector, \vec{R}_1 defines the z^{BF} axis and the $(x, z; z > 0)$ half-plane in the BF is defined such that \vec{R}_2 is within this half-plane. Since $\theta_1 = \varphi_1 = \varphi_2 = 0$ in this BF frame, there are nine internal coordinates $(R_1, R_2, R_3, R_4, u_2, u_3, u_4, \varphi_3, \varphi_4)$, where R_i is the bond distance of each valence vector \vec{R}_i , $\theta_{i=2,3,4}$ are defined as the polar angles between $\vec{R}_{i=2,3,4}$ and \vec{R}_1 . The angles $\varphi_{i=3,4}$ are the spherical dihedral angles of $\vec{R}_{i=3,4}$ in the BF frame. The TANA program⁸⁷⁻⁸⁹ was used to

generate the KEO terms, which are also given in SI in the machine readable format. Note that a subgroup permutation symmetry can be easily imposed with this coordinate system. The transformations of the nine coordinates under the CNPI operations in this coordinate system are given in SI, but they are not implemented here because the dissociation dynamics is restricted to the O-H bond cleavage.

D. Numerical Details

We used DVR⁸¹ as the primitive basis and some coordinates are combined together. The details of the grid parameters, mode combinations and numbers of SPFs are summarized in Table I and Table II for NH₃ and CH₂OH, respectively. The mode combinations are given in the Tables, for example, (r_1, r_2) means that r_1 and r_2 were combined into a composite mode. Specifically for NH₃, we have three two-coordinate modes (r_1, r_2) , (u_1, u_2) , and (r_3, ϕ) . For CH₂OH, five modes R_1 , (R_2, u_2) , (R_3, R_4) , (u_3, ϕ_3) and (u_4, ϕ_4) were used.

The number of sampling points in the MCCPD decomposition of the DPEMs, as well as those for testing the quality of refits, are listed in Table III. As discussed above, we prefer uniform sampling in some coordinates, as opposed to the Metropolis sampling recommended in previous work,⁴⁹ because the dynamical relevant region in our cases covers a relatively larger configuration space than that is needed for vibrational energy level calculations. So, the strategy here is to define the dynamically relevant region, in which each coordinate is limited to a certain range and those points with energies higher

than a threshold are excluded. Then, the points are sampled uniformly within the dynamical region. In some cases, the sampling is augmented by Metropolis sampling to improve the description of energy minima. The ultimate convergence of the refitting was checked with the convergence of dynamic properties such as the absorption spectrum and product branching ratio.

For NH_3 , the ground electronic state PES is dominated by a double well along the inversion of the NH_3 umbrella coordinate. Since the tunneling splitting of the lowest vibrational level is sensitive to the quality of the ground state PES, some points were selected using the Metropolis sampling to provide an optimal description of the PESs near its ground state minima. This group of points, which is denoted in Table III as Sampling 1, was augmented with second group of points that were obtained by uniform sampling, denoted as Sampling 2. Additional points were added to cover the dissociation channels, and they are denoted as Sampling 3. All three groups of points were used in the MCCPD fitting. For CH_2OH , a single region was defined and all grids were uniformly sampled. As shown in our previous work on CH_2OH photodissociation,⁷⁶ most modes are inactive thus only relative small ranges of grids were needed.

The standard constant mean-field (CMF) integration scheme²⁸ implemented in the Heidelberg MCTDH code⁹⁰ was used with the short-iterative Lanczos integrator⁹¹ to propagate the time-dependent expansion coefficients and Bulirsch–Stoer (BS) method to propagate the SPFs. Complex absorption potentials (CAPs)⁹² were placed near the edges

of the dissociative coordinate, namely r_1, r_2, r_3 for NH_3 and R_2, R_3, R_4 for CH_2OH . The absorption spectrum was calculated from the Fourier transfer of the time-dependent autocorrelation function. The flux to the product asymptote was analyzed based on the CAPs⁴² to obtain the branching ratio for NH_3 . The energy spectrum of the flux was obtained by Fourier transform.⁴² The initial wave functions, namely the eigenfunctions on the ground electronic state, were obtained by a relaxation method^{93, 94} for both NH_3 and CH_2OH , in which the wave packet was propagated in imaginary time. The influence of the transition dipole is ignored within the Condon approximation. All the calculations were done using the Heidelberg MCTDH Package.⁹⁰

III. Results and Discussion

NH_3

To test the accuracy of the MCTDH method in treating nonadiabatic photodissociation dynamics, we focus on two quantities, namely the absorption spectrum and product branching ratio. The MCTDH results are compared with those obtained using a grid method with the Chebyshev propagator⁹⁵ (denoted below as Chebyshev), as reported in our earlier publications.^{63, 64} The grid-based Chebyshev method is considered exact because of the exponential convergence properties of the DVR grid and Chebyshev propagator.^{96, 97}

The fitting quality of the DEPM is given in the Table V. As mentioned above, the MCCPD fitting for NH_3 was done with three groups of sampling points. On the ground state PES, the energy splitting of the tunneling doublet was calculated to be 0.67 cm^{-1} ,

which agrees well with the experimental value (0.793 cm^{-1})⁹⁸ and the theoretical value (0.45 cm^{-1}) obtained on the original PES⁶³ by a grid based method. We emphasize that the clear resolution of the small splitting is made possible by our ability to impose the CNPI symmetry in the MCCPD PES and the MCTDH wave packet, which allows separate calculations with different parities. The minor difference between the MCTDH and Chebyshev values is presumably due to the remaining errors in transforming the original ground state PES into the SOP form.

The absorption spectrum of NH_3 features a series of peaks with finite widths due to long-lived resonances in the umbrella vibration, thanks to the pyramidal-to-planar transition. These Feshbach resonances are above both dissociation limits ($\text{H} + \text{NH}_2(\text{X})/\text{NH}_2(\text{A})$), but energy flow to the dissociation coordinate is slow. The long lifetime of these resonances made the MCTDH treatment challenging because of the accumulation of errors in a long propagation. Indeed, the previous MCTDH study of the same system failed to reproduce quantitatively the absorption spectrum,⁶⁰ presumably due to the lack of symmetry in the coordinates used. Figure 2(a) shows the comparison of the absorption spectrum obtained from the MCTDH calculation and the previous Chebyshev method⁶³ for even parity levels. (The agreement with the odd parity levels is equally good, but not shown here.) This agreement is almost perfect, which demonstrates the accuracy of both the refitted DPEM and the MCTDH propagation. Here, we emphasize that the symmetry of

the DPEM has been correctly treated so the parity is conserved in the propagation, evidenced by the absence of peaks for the odd parity levels in Figure 2(a).

Figure 2(b) shows the comparison of product branching ratio ($\text{NH}_2(\text{A}) / \text{NH}_2(\text{X})$) ranged from 6.5 to 8.0 eV between the MCTDH and Chebyshev results. The black arrows indicate the peak positions in the absorption spectrum. The overall agreement is satisfactory especially near the peaks, but the MCTDH result is more oscillatory. The errors are mostly near the spectral troughs, suggesting uneven performance of MCTDH in spectral regions with small amplitude.

To gain insights into the origin of the errors, we plot the energy spectra for both the $\text{NH}_2(\text{X})$ and $\text{NH}_2(\text{A})$ channels in Figure 3, the ratio of which gives the product branching ratio shown in Figure 2(b). It is clear that the energy spectrum for the $\text{NH}_2(\text{A})$ channel is in good agreement with the Chebyshev results, but the agreement for the $\text{NH}_2(\text{X})$ channel is not as good, particularly in the troughs where a background is present in comparison with the Chebyshev method. We attribute the errors in the $\text{NH}_2(\text{X})$ channel to the multiple crossings at the CI seam, because of the long-lived nature of the resonances. The huge phase space accessible in the ground state would require a large number of SPFs to converge the flux calculation, which we cannot afford due to much increased computational costs. To confirm this hypothesis, we performed a calculation without the off-diagonal coupling terms in the DPEM to approximate the dissociation dynamics on the diabatic PES V_{22} . The corresponding spectrum is also displayed in Figure 3(a). Since V_{11}

is not involved in this hypothetical diabatic dynamics, the dissociation is fast and the spectrum is well converged comparing with the Chebyshev result. This is further confirmed by the much smaller population of the higher natural orbital in the single PES calculation than the coupling DPEM results, as shown in Table IV.

CH₂OH

The fitting quality of the CH₂OH DPEM can be found in Table V. Figure 4 displays the calculated absorption spectrum as a function of photon energy using a full-dimensional MCTDH model covering all nine internal DOFs. The agreement with the experiment⁷⁸ is reasonable within the measured range. The agreement is also quite satisfactory with our previous result,⁷⁵ which used a four-dimensional (4D) grid based model. The absorption spectrum of CH₂OH is quite broad due to the fast dissociation dynamics on the largely repulsive excited state PES, which several weak resonance peaks superimposed on the broad background.⁷⁵ These general features are reproduced by the 9D MCTDH spectrum. The small but recognizable shift relative to the 4D spectrum can be rationalized by the difference of zero-point energies of the ground and excited states when more DOFs are included.

As pointed out in our previous work,⁷⁵ the dissociating wave packet makes facile nonadiabatic transitions near the CI seam, which is located within the Franck-Condon region. The residual population on the upper diabatic state revisits the Franck-Condon region and the weak recurrence in the autocorrelation function leads to the broad

resonances.⁷⁵ The energy gap between the weak resonance peaks corresponds to the stretching of the C-O bond, which is significantly shorter on the excited electronic state than the ground state due to the $n\leftarrow\pi^*$ transition.⁷⁵ Indeed, the absorption spectrum with the off-diagonal DPEM terms switched off has no such structure, as shown in the same figure, underscoring the importance of nonadiabatic transitions.

Figure 5 displays the time evolution of populations in the two diabatic states (labeled as P_2 and P_1), with comparison with those obtained in the 4D Chebyshev calculation.⁷⁵ P_2 decays rapidly, which reflects the fast nonadiabatic transitions to the lower state and the weak recurrence can also be seen near 20 and 50 fs. The nonadiabatic population transfer is completed within 100 fs, evidenced by the vanishing P_2 . Hence, all dissociation is expected to yield the $H + H_2CO(X)$ products. This is qualitative consistent with the 4D model, suggesting the validity of the reduced-dimensional model. The slow decay of P_1 after 10 fs is artificial due to the absorption of the wave packet by the CAPs at the large R region.

IV. Conclusions

In this work, we performed full quantum dynamics investigations on two prototypical nonadiabatic photodissociation systems using the MCTDH method, made possible by the recently proposed MCCPD method for expressing the PEO in the SOP form. One such system is the photodissociation of NH_3 in the first band, a relatively small but difficult system to deal with by MCTDH, due to the presence of long-lived resonances. For this

system, the absorption spectrum calculated using the exact Chebyshev method is reproduced with near perfection, which represents a significant improvement over the previous MCTDH treatment. In addition, the agreement on the branching ratio is satisfactory. Detailed analysis suggests a much larger number of SPFs might be needed to provide quantitatively accurate results, due apparently to the chaotic dynamics in the huge phase space of the ground state and the long lifetime of the resonances. The other system, namely the photodissociation of CH₂OH in the 3*s* Rydberg state, is challenging with nine DOFs. In contrast to the NH₃ case, the non-adiabatic dynamics is fast, leading to a broad absorption spectrum superimposed with weak resonance peaks. The full-dimensional results validate the earlier reduced-dimensional models. These studies lay the foundation of the future extension of the MCTDH treatment of nonadiabatic photodissociation dynamics to the state-to-state level where the product state distribution is resolved.

Acknowledgements: This work was supported by the Department of Energy (DF-FG02-05ER15694 to DRY and HG). We thank Prof. C. Xie for numerous discussions. The calculations were performed at the Center for Advanced Research Computing (CARC) at UNM.

Table I. Parameters for the primitive basis for NH₃. More details about the DVR bases can be found in Appendix B in Ref. ²⁸.

Coordinate	Range	Grid points	Primitive basis	Mode combination	Number of SPFs (State 1, State 2)
r_1	1.3~ 4.5 Bohr	18	HO-DVR	(r_1, r_2)	(35, 35)
r_2	1.3~ 4.5 Bohr	18	HO-DVR		
u_1	-0.95~ 0.8	25	HO-DVR	(u_1, u_2)	(65, 65)
u_2	-0.95~ 0.8	25	HO-DVR		
r_3	1,3~ 8.0 Bohr	55	Sine-DVR	(r_3, ϕ)	(95, 120)
ϕ	0~ 2π	50	HO-DVR		

Table II. Parameters for the primitive basis sets for CH₂OH. More details about the DVR

bases can be found in Appendix B in Ref. ²⁸.

Coordinate	Range	Grid points	Primitive basis	Mode combination	Number of SPFs (State 1, State 2)
R_1	1.7~ 3.5 Bohr	16	HO-DVR	R_1	(12, 12)
R_2	1.2~8.0 Bohr	80	sine-DVR	(R_2, u_2)	(25, 25)
u_2	-0.75~ 0.98	25	sine-DVR		
R_3	1.3~ 4.0 Bohr	36	sine-DVR	(R_3, R_4)	(15, 15)
R_4	1.3~ 4.0 Bohr	36	sine-DVR		
u_3	-0.95~0.65	25	sine-DVR	(u_2, ϕ_3)	(20, 20)
ϕ_3	0~ 2π Rad.	50	sine-DVR		
u_4	-0.95~0.65	25	sine-DVR	(u_4, ϕ_4)	(20, 20)
ϕ_4	0~ 2π Rad.	50	sine-DVR		

Table III. Sampling methods, points for decomposing the DEPM of NH₃ and CH₂OH.

Note for each sampling group, the larger number in parentheses are used for testing the fitting quality.

<p>NH₃:</p> <p>Sampling 1: 30000 (300000) points, Metropolis, $k_B T = 1000 \text{ cm}^{-1}$ for V_{11} 30000 (300000) points, Metropolis, $k_B T = 62589 \text{ cm}^{-1}$ for V_{22} 10000 (100000) points, Metropolis, $k_B T = 2000 \text{ cm}^{-1}$ for V_{12}</p> <p>Sampling 2: 100000 (1000000) points, uniform for V_{11}, V_{22} and V_{12}. Threshold < 10 eV</p> <p>Sampling 3: 90000 (900000) points, uniform, dynamical region r_1 and r_2 [1.7, 3.4] Bohr, r_3 [1,4, 8.0] Bohr, u_1 and u_2 [-0.6, 0.0], ϕ [2,2, 4.08] Rad. Threshold < 10 eV</p> <p>CH₂OH:</p> <p>Sampling : 80000 (1000000), points, uniform dynamical region, R_1 [2.3, 3.9] Bohr, R_2[1.3, 8.1] Bohr, R_3 and R_4 [1.6, 2.8] Bohr, u_2 [0.0, 0.6], u_3 and u_4 [-0.6, 0.4], ϕ_3[2.0 3.7] Rad., ϕ_4[5.0 2π] Rad. and ϕ_4 [0, 1.0] Rad. Threshold < 8 eV</p>

Table IV. Maximum population over time of the highest natural orbital in NH_3 photodissociation.

Mode	Diabatic state 1	Diabatic state 2	Single diabatic state without coupling
(r_1, r_2)	4.2×10^{-5}	2.5×10^{-5}	6.5×10^{-6}
(r_3, ϕ)	1.5×10^{-4}	6.5×10^{-5}	3.9×10^{-7}
(u_1, u_2)	1.9×10^{-4}	1.5×10^{-4}	1.1×10^{-5}

Table V. Fitting errors (cm^{-1}) for decomposing the DEPMs of NH_3 and CH_2OH . The root

mean square error (RMSE) is defined as $\sqrt{\frac{1}{N_C} \sum_s (V_s - V_s^{CPD})^2}$, where N_C is total number

of testing points given in Table III, and the subscript s is the index for each testing grid.

NH_3	RMSE Sampling 1	RMSE Sampling 2	RMSE Sampling 3	RMSE Total
V_{11}	15.7	270	92.2	191
V_{22}	411	501	90.9	371
V_{12}	501	365	43.1	283

CH_2OH	RMSE
V_{11}	141.05
V_{22}	73.97
V_{12}	78.87

Reference

1. M. Born and K. Huang, *Dynamical Theory of Crystal Lattices*. (Clarendon, Oxford, 1954).
2. A. W. Jasper, B. K. Kendrick, C. A. Mead and D. G. Truhlar, in *Modern Trends in Chemical Reaction Dynamics: Experiment and Theory*, edited by X. Yang and K. Liu (World Scientific, Singapore, 2004), Vol. 1, pp. 329-391.
3. M. Baer, *Beyond Born-Oppenheimer: Electronic Nonadiabatic Coupling Terms and Conical Intersections*. (Wiley, New Jersey, 2006).
4. D. R. Yarkony, Chem. Rev. **112**, 481-498 (2011).
5. W. Domcke and D. R. Yarkony, Annu. Rev. Phys. Chem. **63**, 325-352 (2012).
6. H. Köppel, W. Domcke and L. S. Cederbaum, Adv. Chem. Phys. **57**, 59-246 (1984).
7. W. Domcke, D. R. Yarkony and H. Köppel, (World Scientific, Singapore, 2011).
8. C. A. Mead, Rev. Mod. Phys. **64**, 51-85 (1992).
9. C. Xie, C. L. Malbon, H. Guo and D. R. Yarkony, Acc. Chem. Res. **52**, 501-509 (2019).
10. F. Bernardi, M. Olivucci and M. A. Robb, Chem. Soc. Rev. **25**, 321-328 (1996).
11. B. G. Levine and T. J. Martínez, Annu. Rev. Phys. Chem. **58**, 613-634 (2007).
12. S. Matsika and P. Krause, Annu. Rev. Phys. Chem. **62**, 621-643 (2011).
13. T. R. Nelson, A. J. White, J. A. Bjorgaard, A. E. Sifain, Y. Zhang, B. Nebgen, S. Fernandez-Alberti, D. Mozyrsky, A. E. Roitberg and S. Tretiak, Chem. Rev. **120**, 2215-2287 (2020).
14. G. G. Balint-Kurti and M. Shapiro, in *Photodissociation and Photoionization*, edited by K. P. Lawley (Wiley, New York, 1985), pp. 403-450.
15. M. N. R. Ashfold and J. E. Baggott, *Molecular Photodissociation Dynamics*. (The Royal Society of Chemistry, London, 1987).
16. R. Schinke, *Photodissociation Dynamics*. (Cambridge University Press, Cambridge, 1993).
17. L. J. Butler and D. M. Neumark, J. Phys. Chem. **100**, 12801-12816 (1996).
18. M. N. R. Ashfold, G. A. King, D. Murdock, M. G. D. Nix, T. A. A. Oliver and A. G. Sage, Phys. Chem. Chem. Phys. **12**, 1218-1238 (2010).
19. K. Yuan, R. N. Dixon and X. Yang, Acc. Chem. Res. **44**, 369-378 (2011).
20. H. Guo and D. R. Yarkony, Phys. Chem. Chem. Phys. **18**, 26335-26352 (2016).
21. X. Hu, L. Zhou and D. Xie, WIREs Comput. Mol. Sci., e1350 (2017).
22. J. Behler, J. Phys. Condens. Mat. **26**, 183001 (2014).
23. C. Qu, Q. Yu and J. M. Bowman, Annu. Rev. Phys. Chem. **69**, 151-175 (2018).
24. B. Jiang, J. Li and H. Guo, J. Phys. Chem. Lett. **11**, 5120-5131 (2020).
25. J. Westermayr and P. Marquetand, Chem. Rev. **121**, 9873-9926 (2021).
26. Y. Guan, C. Xie, D. R. Yarkony and H. Guo, Phys. Chem. Chem. Phys. **23**, 24962-24983 (2021).

27. Y. Shu, Z. Varga, S. Kanchanakungwankul, L. Zhang and D. G. Truhlar, *J. Phys. Chem. A* **126**, 992–1018 (2022).
28. M. H. Beck, A. Jackle, G. A. Worth and H.-D. Meyer, *Phys. Rep.* **324**, 1-105 (2000).
29. H.-D. Meyer, F. Gatti and G. A. Worth, *Multidimensional Quantum Dynamics: MCTDH Theory and Applications*. (Wiley-VCH, 2009).
30. H.-D. Meyer, *WIRES: Comput. Mol. Sci.* **2**, 351-374 (2012).
31. H.-D. Meyer, U. Manthe and L. S. Cederbaum, *Chem. Phys. Lett.* **165**, 73-78 (1990).
32. U. Manthe, H.-D. Meyer and L. S. Cederbaum, *J. Chem. Phys.* **97**, 3199-3213 (1992).
33. H. Wang and M. Thoss, *J. Chem. Phys.* **119**, 1289-1299 (2003).
34. M. Schröder, F. Gatti and H.-D. Meyer, *J. Chem. Phys.* **134**, 234307 (2011).
35. Q. Meng and H.-D. Meyer, *J. Chem. Phys.* **138**, 014313 (2013).
36. R. Ellerbrock and U. Manthe, *J. Chem. Phys.* **148**, 224303 (2018).
37. R. Binder, D. Lauvergnat and I. Burghardt, *Phys. Rev. Lett.* **120**, 227401 (2018).
38. W. Popp, M. Polkehr, R. Binder and I. Burghardt, *J. Phys. Chem. Lett.* **10**, 3326-3332 (2019).
39. Q. Meng, M. Schröder and H.-D. Meyer, *J. Chem. Theo. Comput.* **17**, 2702-2713 (2021).
40. R. van Harrevelt and U. Manthe, *J. Chem. Phys.* **123**, 064106 (2005).
41. R. Wodraszka and T. Carrington, *J. Chem. Phys.* **148**, 044115 (2018).
42. A. Jäckle and H.-D. Meyer, *J. Chem. Phys.* **104**, 7974-7984 (1996).
43. A. Jäckle and H.-D. Meyer, *J. Chem. Phys.* **109**, 3772-3779 (1998).
44. D. Peláez and H.-D. Meyer, *J. Chem. Phys.* **138**, 014108 (2013).
45. F. Otto, *J. Chem. Phys.* **140**, 014106 (2014).
46. M. Schröder and H.-D. Meyer, *J. Chem. Phys.* **147**, 064105 (2017).
47. F. Otto, Y.-C. Chiang and D. Peláez, *Chem. Phys.* **509**, 116-130 (2018).
48. L. R. Tucker, *Psychometrika* **31**, 279-311 (1966).
49. M. Schröder, *J. Chem. Phys.* **152**, 024108 (2020).
50. S. Ndengué, Y. Scribano, F. Gatti and R. Dawes, *J. Chem. Phys.* **151**, 134301 (2019).
51. H. Köppel, M. Döscher, I. Báldea, H. D. Meyer and P. G. Szalay, *J. Chem. Phys.* **117**, 2657-2671 (2002).
52. A. Raab, G. A. Worth, H.-D. Meyer and L. S. Cederbaum, *J. Chem. Phys.* **110**, 936-946 (1998).
53. A. Markmann, G. A. Worth, S. Mahapatra, H.-D. Meyer, H. Köppel and L. S. Cederbaum, *J. Chem. Phys.* **123**, 204310 (2005).
54. G. A. Worth, H. D. Meyer, H. Köppel, L. S. Cederbaum and I. Burghardt, *Int. Rev. Phys. Chem.* **27**, 569-606 (2008).
55. S. Mahapatra, G. A. Worth, H. D. Meyer, L. S. Cederbaum and H. Köppel, *J. Phys. Chem. A* **105**, 5567-5576 (2001).
56. J.-Y. Fang and H. Guo, *Chem. Phys. Lett.* **235**, 341-346 (1995).

57. L. Liu, J.-Y. Fang and H. Guo, *J. Chem. Phys.* **102**, 2404 (1995).
58. A. Viel, R. P. Krawczyk, U. Manthe and W. Domcke, *J. Chem. Phys.* **120**, 11000-11010 (2004).
59. C. R. Evenhuis and U. Manthe, *J. Phys. Chem. A* **115**, 5992-6001 (2011).
60. K. Giri, E. Chapman, C. S. Sanz and G. Worth, *J. Chem. Phys.* **135**, 044311 (2011).
61. S. A. Ndengue, R. Schinke, F. Gatti, H.-D. Meyer and R. Jost, *J. Phys. Chem. A* **116**, 12271-12279 (2012).
62. W. Lai, S. Y. Lin, D. Xie and H. Guo, *J. Chem. Phys.* **129**, 154311 (2008).
63. X. Zhu, J. Ma, D. R. Yarkony and H. Guo, *J. Chem. Phys.* **136**, 234301 (2012).
64. J. Ma, X. Zhu, H. Guo and D. R. Yarkony, *J. Chem. Phys.* **137**, 22A541 (2012).
65. J. Ma, C. Xie, X. Zhu, D. R. Yarkony, D. Xie and H. Guo, *J. Phys. Chem. A* **118**, 11926-11934 (2014).
66. C. Xie, J. Ma, X. Zhu, D. H. Zhang, D. R. Yarkony, D. Xie and H. Guo, *J. Phys. Chem. Lett.* **5**, 1055-1060 (2014).
67. C. Xie, X. Zhu, J. Ma, D. R. Yarkony, D. Xie and H. Guo, *J. Chem. Phys.* **142**, 091101 (2015).
68. Z. H. Li, R. Valero and D. G. Truhlar, *Theo. Chem. Acc.* **118**, 9-24 (2007).
69. V. Vaida, M. I. McCarthy, P. C. Engelking, P. Rosmus, H.-J. Werner and P. Botschwina, *J. Chem. Phys.* **86**, 6669-6676 (1987).
70. J. Biesner, L. Schnieder, G. Ahlers, X. Xie, K. H. Welge, M. N. R. Ashfold and R. N. Dixon, *J. Chem. Phys.* **91**, 2901-2911 (1989).
71. D. H. Mordant, M. N. R. Ashfold and R. N. Dixon, *J. Chem. Phys.* **104**, 6460-6471 (1996).
72. A. Bach, J. M. Hutchison, R. J. Holiday and F. F. Crim, *J. Chem. Phys.* **118**, 7144-7145 (2003).
73. M. L. Hause, Y. H. Yoon and F. F. Crim, *J. Chem. Phys.* **125**, 174309 (2006).
74. J. D. Rodriguez, M. G. Gonzalez, L. Rubio-Lago and L. Banares, *Phys. Chem. Chem. Phys.* **16**, 406-413 (2014).
75. C. Xie, C. Malbon, D. R. Yarkony and H. Guo, *J. Chem. Phys.* **146**, 224306 (2017).
76. C. Xie and H. Guo, *J. Chem. Phys.* **148**, 044305 (2018).
77. C. L. Malbon and D. R. Yarkony, *J. Chem. Phys.* **146**, 134302 (2017).
78. L. Feng, X. Huang and H. Reisler, *J. Chem. Phys.* **117**, 4820-4824 (2002).
79. C. P. Rodrigo, C. Zhou and H. Reisler, *J. Phys. Chem. A* **117**, 12049-12059 (2013).
80. M. Ehara, H.-D. Meyer and L. S. Cederbaum, *J. Chem. Phys.* **105**, 8865 (1996).
81. J. C. Light and T. Carrington Jr., *Adv. Chem. Phys.* **114**, 263-310 (2000).
82. P. R. Bunker and P. Jensen, *Molecular Symmetry and Spectroscopy*. (NRC Research Press, Ottawa, 1998).
83. C. Xie, X. Zhu, D. R. Yarkony and H. Guo, *J. Chem. Phys.* **149**, 144107 (2018).
84. M. J. Bramley and T. Carrington Jr., *J. Chem. Phys.* **99**, 8519-8541 (1993).

85. C. Iung, F. Gatti, A. Viel and X. Chapuisat, *Phys. Chem. Chem. Phys.* **1**, 3377-3385 (1999).
86. F. Gatti, C. Muñoz and C. Iung, *J. Chem. Phys.* **114**, 8275-8281 (2001).
87. M. Ndong, L. Joubert-Doriol, H.-D. Meyer, A. Nauts, F. Gatti and D. Lauvergnat, *J. Chem. Phys.* **136**, 034107 (2012).
88. M. Ndong, A. Nauts, L. Joubert-Doriol, H.-D. Meyer, F. Gatti and D. Lauvergnat, *J. Chem. Phys.* **139**, 204107 (2013).
89. D. Lauvergnat. TNUM-TANA: A fortran code for coordinate transformations and kinetic energy operators. See <https://github.com/lauvergn/EIVibRot-TnumTana>.
90. G. A. Worth, M. H. Beck, A. Jäckle and H.-D. Meyer, MCTDH Package Version 8.5 (University of Heidelberg, 2021).
91. T. J. Park and J. C. Light, *J. Chem. Phys.* **85**, 5870-5876 (1986).
92. U. V. Riss and H.-D. Meyer, *J. Phys.* **B26**, 4503 (1993).
93. R. Kosloff and H. Tal-Ezer, *Chem. Phys. Lett.* **127**, 223-230 (1986).
94. H.-D. Meyer, F. L. Quéré, C. Léonard and F. Gatti, *Chem. Phys.* **329**, 179-192 (2006).
95. H. Guo, *J. Chem. Phys.* **108**, 2466-2472 (1998).
96. R. Kosloff, *Annu. Rev. Phys. Chem.* **45**, 145 (1994).
97. H. Guo, *Rev. Comput. Chem.* **25**, 285-347 (2007).
98. G. Herzberg, *Molecular Spectra and Molecular Structure, Vol. 3, Electronic Spectra of Polyatomic Molecules*. (Van Nostrand, Princeton, 1966).

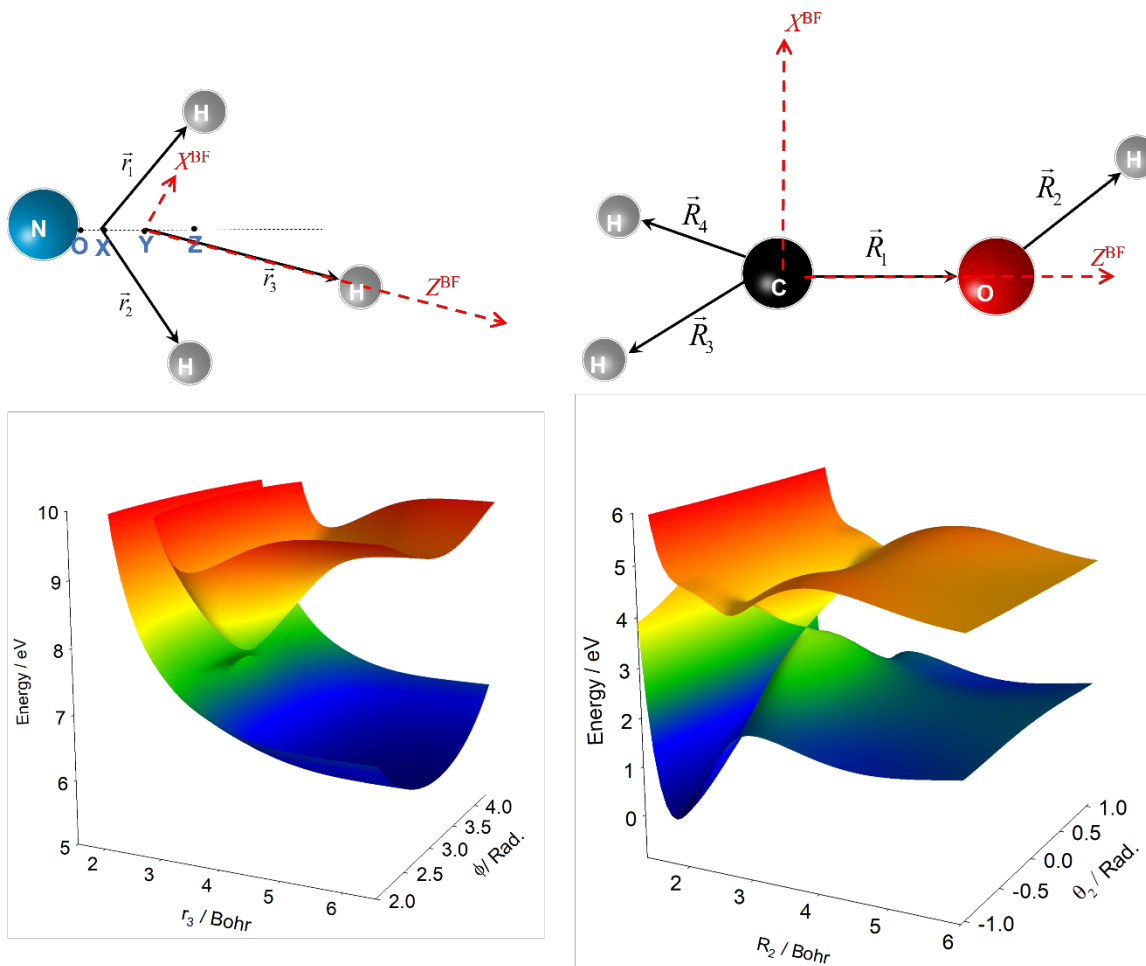


Figure 1. Upper panel: The 2+1 Radau-Jacobi coordinate system used for NH₃ (left) and the valence coordinates for CH₂OH (right). In the former, X is the canonical center of Radau vectors, Y and Z are the NH₂ center of mass and the center of mass of the two H atoms, respectively. The canonical center of Radau vectors is defined as $\overline{XZ}^2 = \overline{OZ} \cdot \overline{YZ}$. In the latter, the origin of the BF frame is defined at C and the C-O axis is along the z^{BF} and O-H axis is contained in the $x^{BF}-z^{BF}$ plane. Lower panel: (left) The adiabatic PESs of the two electronic states of NH₃ in the r_3 and ϕ coordinates with others are fixed at their equilibrium. (Right) The adiabatic PESs of the two electronic states of CH₂OH in the R_2

and θ_2 coordinates with R_1 , R_3 and R_4 fixed at its equilibrium, $\theta_3 = \theta_4 = 2\pi/3$, $\varphi_3 = \pi/2$ and $\varphi_4 = 3\pi/2$, so that θ_2 is an out-of-plane angle of OH bond with respect to the plane defined by CH₂O.

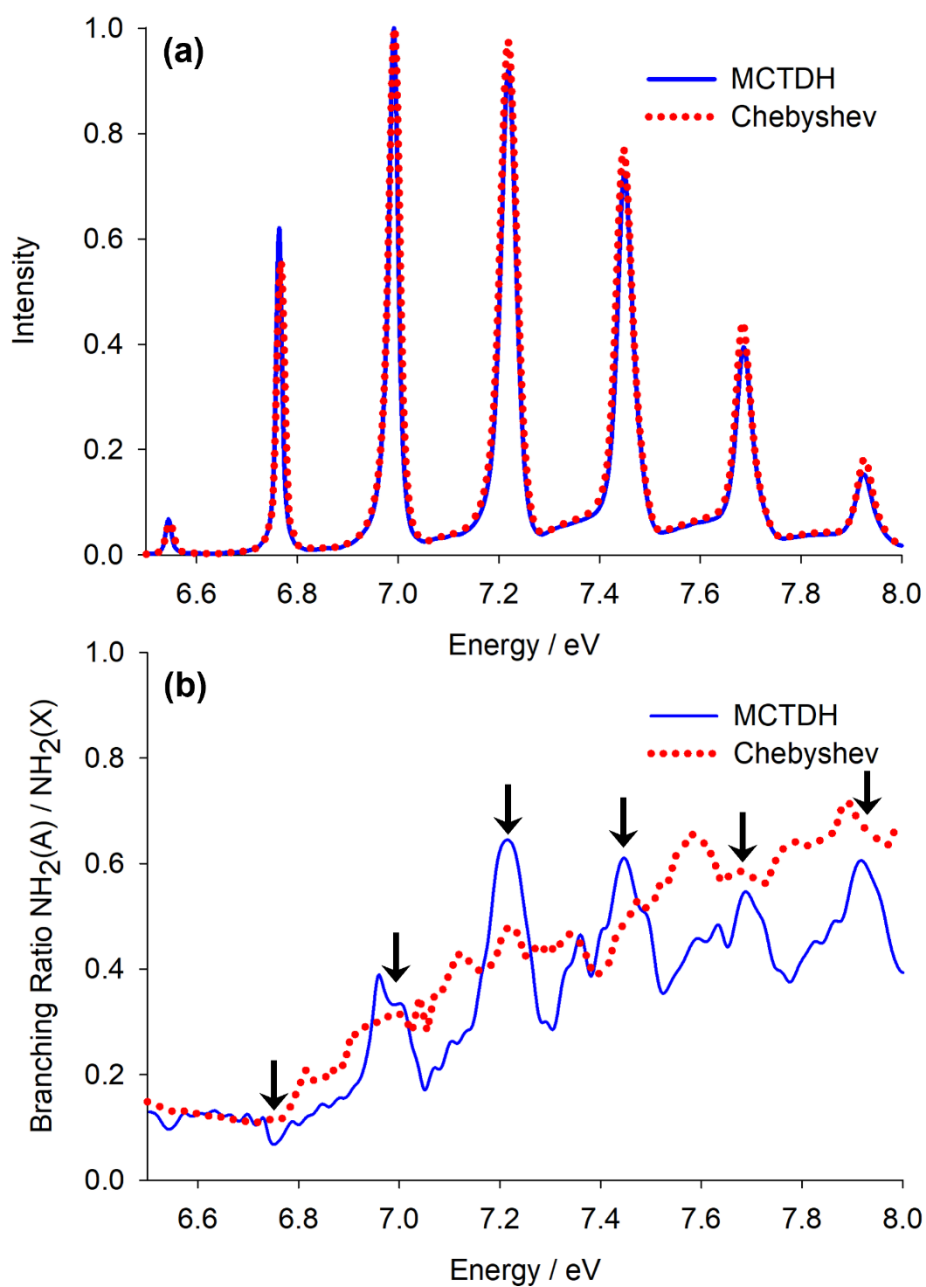


Figure 2. Comparison of the MCTDH absorption spectrum (a) and product branching ratio (b) with the Chebyshev results for NH_3 photodissociation. The absorption spectra in (a) are normalized to the highest peak. The black arrows in (b) indicate the positions of the peaks.

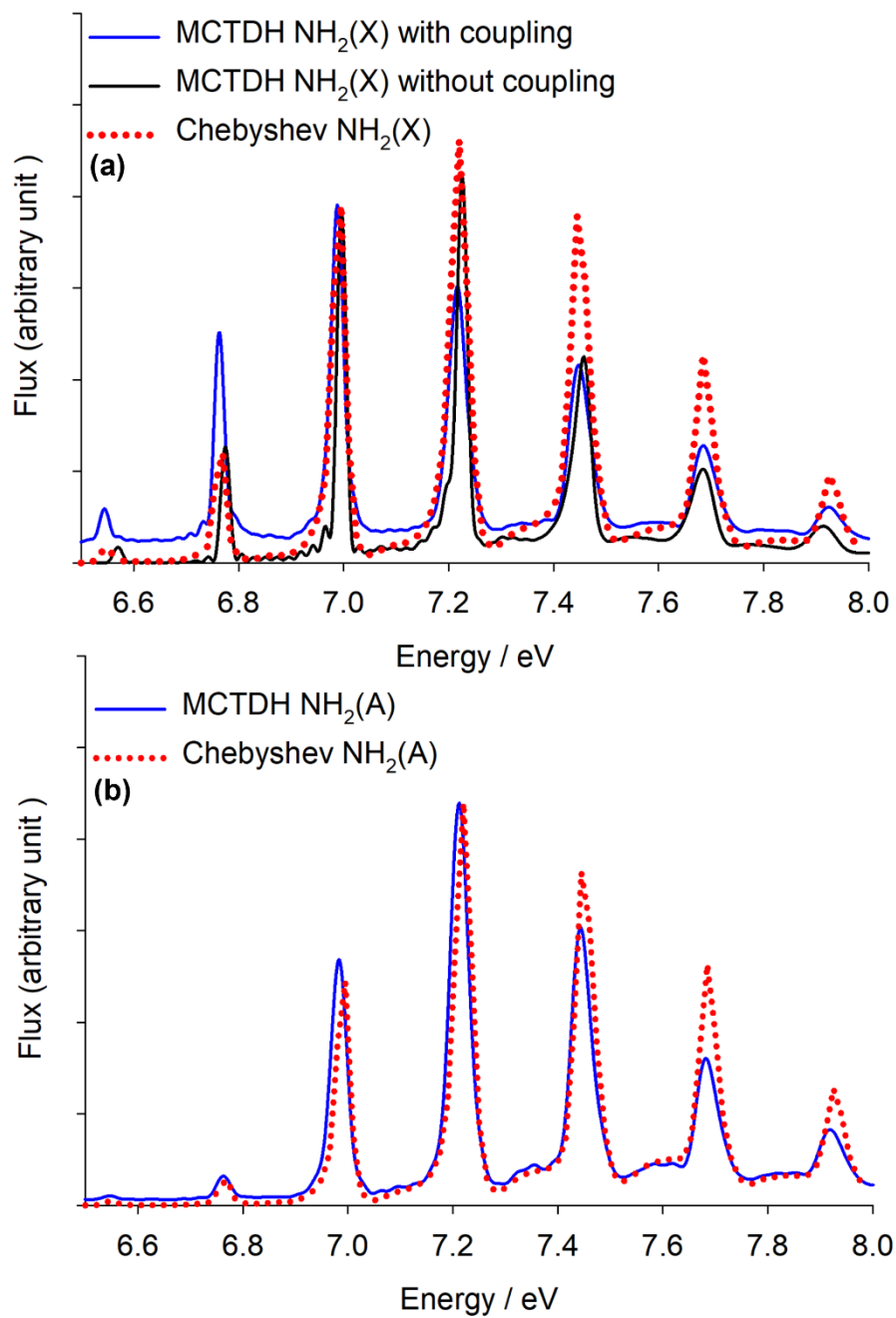


Figure 3. Comparison of the energy spectrum of the MCTDH flux in the $\text{NH}_2(\text{X})$ (a) and $\text{NH}_2(\text{A})$ (b) product channels with the Chebyshev results. The spectra are scaled to the most intensive peak for comparison.

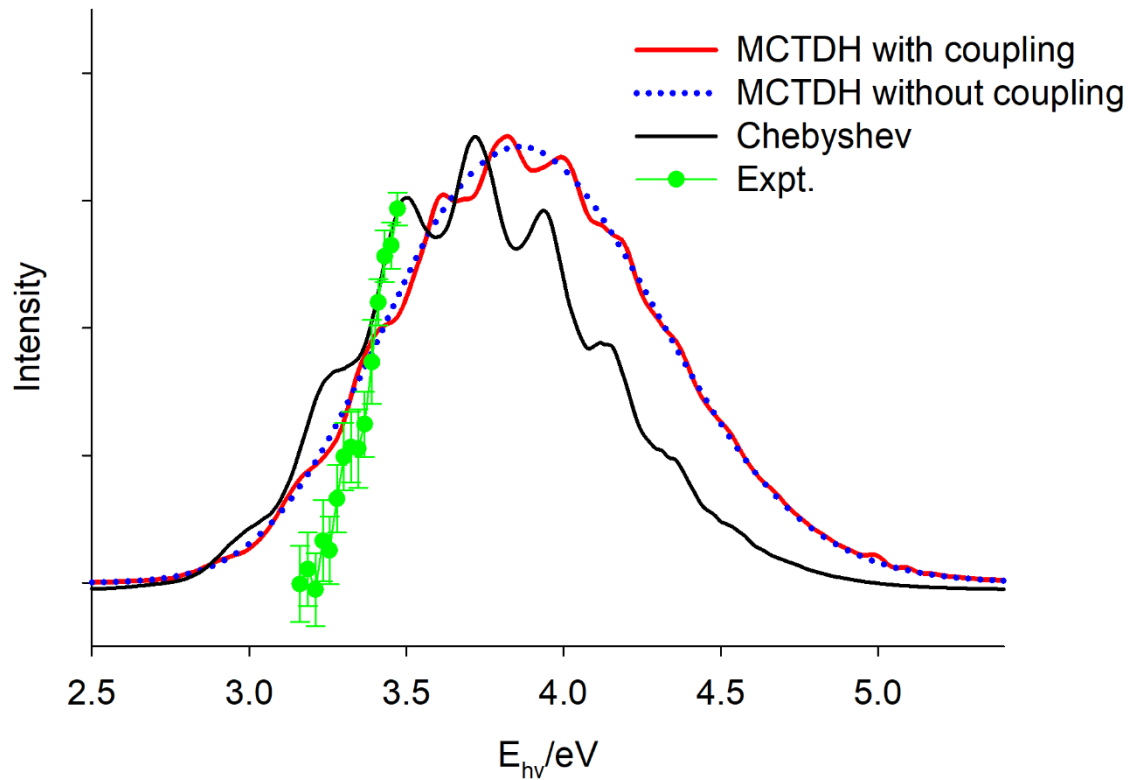


Figure 4. Comparison of the 9D MCTDH absorption spectrum of CH₂OH with a 4D model calculated with the Chebyshev method⁷⁵ with and without the off-diagonal DPEM elements. The experimental absorption spectrum⁷⁸ is also included for comparison. E_{hν} is the photon energy.

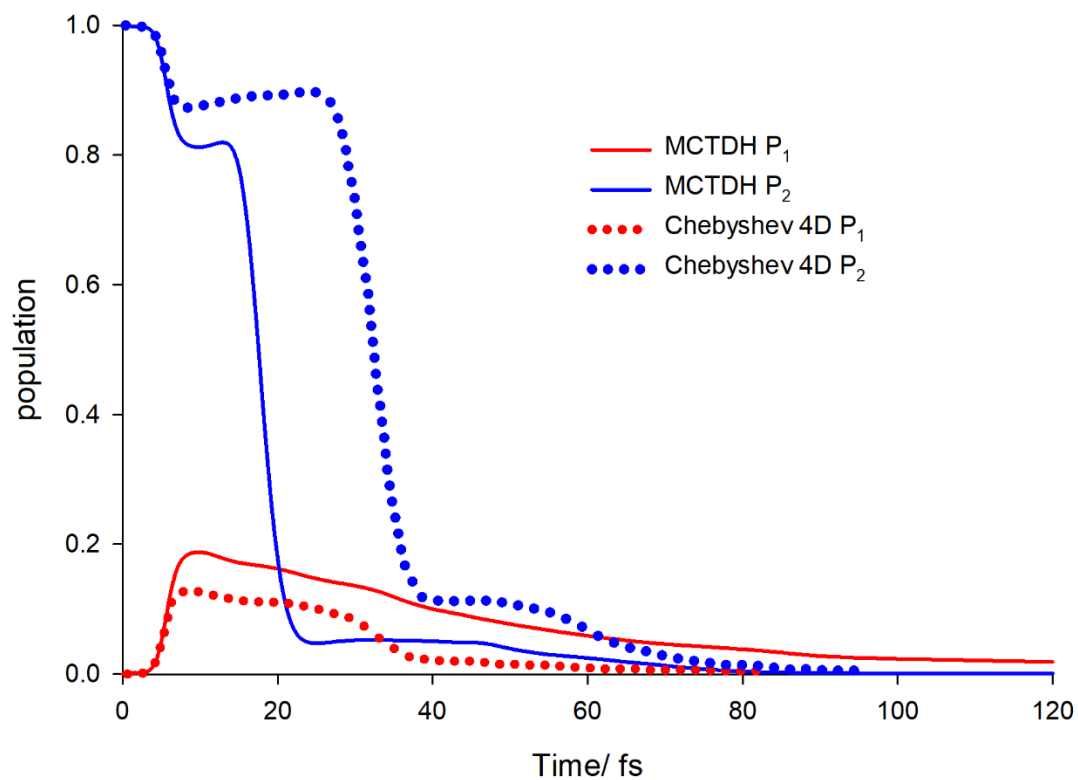


Figure 5. Comparison of the 9D MCTDH populations in two diabatic states of CH_2OH as a function of time with those calculated using a 4D Chebyshev model.⁷⁵